

# Large-scale shell-model calculations for unnatural-parity high-spin states in neutron-rich Cr and Fe isotopes

Tomoaki Togashi<sup>1,\*</sup>, Noritaka Shimizu<sup>1</sup>, Yutaka Utsuno<sup>1,2</sup>, Takaharu Otsuka<sup>1,3,4</sup>, and Michio Honma<sup>5</sup>

<sup>1</sup>*Center for Nuclear Study, University of Tokyo, Hongo, Bunkyo-ku, Tokyo, 113-0033, Japan*

<sup>2</sup>*Advanced Science Research Center, Japan Atomic Energy Agency, Tokai, Ibaraki, 319-1195, Japan*

<sup>3</sup>*Department of Physics, University of Tokyo, Hongo, Bunkyo-ku, Tokyo, 113-0033, Japan*

<sup>4</sup>*National Superconducting Cyclotron Laboratory, Michigan State University, East Lansing, Michigan, 48824, USA*

<sup>5</sup>*Center for Mathematical Sciences, University of Aizu, ikki-machi, Aizu-Wakamatsu, Fukushima, 965-8580, Japan*

(Dated: October 25, 2018)

We investigate unnatural-parity high-spin states in neutron-rich Cr and Fe isotopes using large-scale shell-model calculations. These shell-model calculations are carried out within the model space of  $fp$ -shell +  $0g_{9/2}$  +  $1d_{5/2}$  orbits with the truncation allowing  $1\hbar\omega$  excitation of a neutron. The effective Hamiltonian consists of GXPF1Br for  $fp$ -shell orbits and  $V_{\text{MU}}$  with a modification for the other parts. The present shell-model calculations can describe and predict the energy levels of both natural- and unnatural-parity states up to the high-spin states in Cr and Fe isotopes with  $N \leq 35$ . The total energy surfaces present the prolate deformations on the whole and indicate that the excitation of one neutron into the  $0g_{9/2}$  orbit plays the role of enhancing the prolate deformation. For the positive(unnatural)-parity states in odd-mass Cr and Fe isotopes, their energy levels and prolate deformations indicate the decoupling limit of the particle-plus-rotor model. We have found that the sharp drop of the  $9/2_1^+$  levels in going from  $N = 29$  to  $N = 35$  in odd-mass Cr and Fe isotopes is explained by the Fermi surface approaching the  $\nu 0g_{9/2}$  orbit.

## I. INTRODUCTION

The evolution of the shell structure in neutron-rich nuclei is one of the main interests of modern nuclear physics. The neutron-rich  $fp$ -shell region has attracted particular attraction in this context because new neutron magic numbers have recently been established. The subshell closure at  $N = 32$  is indicated from high  $2_1^+$  levels and reduced  $B(E2, 0_1^+ \rightarrow 2_1^+)$  values in  $^{52}\text{Ca}$  [1, 2],  $^{54}\text{Ti}$  [3, 4], and  $^{56}\text{Cr}$  [5, 6] compared to neighboring isotopes. A new subshell closure at  $N = 34$  was observed in  $^{54}\text{Ca}$  in 2013 [7], more than a decade after its prediction [8]. Evaluating the evolution of those shell gaps is facilitated by advances in shell-model calculations for the full  $fp$ -shell space [9, 10]. The appearance of the  $N = 32$  and  $N = 34$  magic numbers in the proton-deficient region is attributed to the tensor-force driven shell evolution [11].

The evolution of the shell gap at  $N = 40$ , one of the main objectives of this paper, constitutes a key to understanding the characteristic features of the nuclear structure in the neutron-rich  $N \sim 40$  region. While the  $N = 40$  magicity seems to be rather stable in Ni isotopes [12–14], it breaks down completely in Cr and Fe isotopes: very low  $2_1^+$  levels and large  $B(E2, 0_1^+ \rightarrow 2_1^+)$  values in  $^{60-64}\text{Cr}$  [15–18] and  $^{66-68}\text{Fe}$  [15, 18, 19] cannot be reproduced without considerable neutron excitations across the  $N = 40$  shell gap [20–22]. Most recently, it has been reported that the breakdown of the  $N = 40$  magicity can possibly be extended even to Ti isotopes [23] having less proton-neutron quadrupole collectivity than the Cr and

Fe isotopes. This abrupt nuclear-structure change from Ni to lower- $Z$  isotopes is analogous to what is observed in the so-called “island of inversion” region around  $^{32}\text{Mg}$  [24] where neutron excitation induces a large deformation. The evolution of the  $N = 40$  shell gap contributes greatly to the formation of the island of inversion in Cr and Fe isotopes. Indeed, it is suggested in [22] that the  $N = 40$  shell gap reduces with a decreasing proton number in a similar way to the evolution of the  $N = 20$  gap proposed in [25]. The tensor force accounts for this reduction of the harmonic-oscillator shell gaps at  $N = 20$  and 40 toward lower  $Z$ , and also plays a crucial role in the occurrence of the spherical-oblate-prolate shape coexistence in  $^{68}\text{Ni}$  through the Type-II shell evolution proposed in [26].

While the evolution of the  $N = 40$  shell gap thus causes a number of intriguing phenomena, it is very difficult to directly deduce this shell gap from the structure of the Cr and Fe isotopes that belong to the island of inversion. This is because low-lying states of those nuclei are dominated by multi-particle multi-hole excitations, and this property is not very sensitive to small changes of the shell gap. On the other hand, the states dominated by one-particle one-hole ( $1p-1h$ ) excitation provide more direct information on the  $N = 40$  shell gap, when those levels are compared to the  $0p-0h$  states. For Cr and Fe isotopes, low-lying unnatural-parity states with  $N \leq 35$  are regarded as such  $1p-1h$  states because low-lying natural-parity states in this region are excellently described within the  $fp$ -shell configurations [9]. The nuclear properties of unnatural-parity states in Cr and Fe isotopes in the last decade have been measured mainly from  $\gamma$ -ray spectroscopy experiments. Important findings from recent experiments include a sharp drop of the

\* togashi@cns.s.u-tokyo.ac.jp

$9/2_1^+$  levels in going from  $N = 29$  to  $N = 35$  observed in Cr and Fe isotopes [27–31]. If this change in energy level is an indication of a sharp evolution of the  $0g_{9/2}$  orbit with an increasing neutron number as suggested in [20], the driving force of the evolution needs to be clarified.

Another significant nuclear-structure issue in the unnatural-parity states in Cr and Fe isotopes is their nuclear shapes; in particular, how these shapes are polarized by an additional neutron in the  $0g_{9/2}$  orbit. The development of deformation is indicated experimentally from the regular spacing between  $\Delta I = 2$  energy levels observed up to high-spin states [27, 28, 30–32]. While various models show the dominance of prolate deformation in the ground states of Cr isotopes (see [33] for instance), an oblate deformation in the unnatural-parity band of  $^{59}\text{Cr}$  has been suggested in [29] from the observed isomeric  $9/2^+$  state located at 503 keV, which should be the lowest among unnatural-parity states. This level is interpreted naively as the bandhead of the  $K = 9/2$  intrinsic state, which appears to be the lowest for oblate deformation. On the other hand, a recent study with a projected shell-model calculation has shown that prolate deformation is favored based on comparison with experimental data [34]. A similar isomeric  $9/2^+$  state is observed in  $^{61}\text{Fe}$ , and its magnetic moment [35] and absolute value of quadrupole moment [36] support prolate deformation according to the particle-triaxial-rotor model [31]. More elaborate systematic calculations incorporating various degrees of freedom for deformation and configuration help draw a definite conclusion about the shape evolution in Cr and Fe isotopes.

In this paper, we report on systematic large-scale shell-model calculations for natural-parity and unnatural-parity states in Cr and Fe isotopes for  $N \leq 35$ , by clarifying the structure of their  $0p-0h$  and  $1p-1h$  bands. Using a combination of known effective interactions that are slightly modified, we achieve excellent agreement with experiment in the whole region studied. This highly descriptive power enables extracting shell and shape evolutions in this region. This paper is organized as follows. In Sec. II, we present our theoretical framework including the effective Hamiltonian to be used in this work. In Sec. III, first, we show the results of the energy levels for neutron-rich Cr and Fe isotopes; secondly, we discuss the deformation for the natural- and unnatural-parity states in these nuclei. In Sec. IV, we discuss how the  $\nu 0g_{9/2}$  orbit evolves in this mass region by using theoretical and experimental information. Conclusions of this study are given in Sec. V.

## II. THEORETICAL FRAMEWORK

### A. Shell-model calculation

In the mass region of  $Z$  or  $N$  from 20 to 40, the natural-parity states with  $\pi = +(-)$  for even(odd)-mass nuclei are usually described well within the  $fp$ -shell model space

with the  $^{40}\text{Ca}$  inert core. However, the unnatural-parity states with  $\pi = -(+)$  for even(odd)-mass nuclei cannot be described within one major  $fp$  shell. In the quasi-SU3 model [37], the pairs of  $\Delta j = 2$  orbits of a major shell describe quadrupole collectivity. Hence, we choose the  $0g_{9/2}$  and  $1d_{5/2}$  orbits and add them to the  $fp$ -shell model space. In the present shell-model calculation, the model space is composed of  $fp$ -shell ( $0f_{7/2}, 0f_{5/2}, 1p_{3/2}, 1p_{1/2}$ ) +  $0g_{9/2} + 1d_{5/2}$  orbits. To focus on the states dominated by  $1p-1h$  excitation across the  $N = 40$  shell gap, a truncation is introduced so that one neutron is allowed to occupy the  $0g_{9/2}$  or  $1d_{5/2}$  orbit, which means that the  $1\hbar\omega$  excitation of a neutron to the  $gds$  shell occurs in only unnatural-parity states.

The present shell-model Hamiltonian has the following form which consists of one- and two-body terms:

$$H = \sum_i \varepsilon_i c_i^\dagger c_i + \sum_{i < j, k < l} V_{ijkl} c_i^\dagger c_j^\dagger c_l c_k + \beta_{c.m.} H_{c.m.}, \quad (1)$$

where  $\varepsilon_i$  and  $V_{ijkl}$  represent the bare single-particle energy and the two-body matrix element, respectively,  $c_i^\dagger(c_i)$  denotes a creation(annihilation) operator of a nucleon in a single-particle orbit  $i$ , and  $\beta_{c.m.} H_{c.m.}$  is the term proposed by Gloeckner and Lawson to remove the spurious center-of-mass motion due to the excitation beyond one major shell [38]. The parameter of  $\beta_{c.m.}$  is applied as  $\beta_{c.m.} \hbar\omega/A = 10$  MeV, where  $A$  is the mass number:  $A = Z + N$ . We take  $\hbar\omega$  from the empirical value:  $\hbar\omega = 41.0A^{-1/3}$  MeV.

In the present work, the Hamiltonian matrix with an  $M$  scheme is diagonalized by the thick-restart Lanczos method with MSHELL64 code [39] for the dimension of the matrix below  $10^9$  and KSHELL code [40] for the dimension over  $10^9$ .

### B. The effective Hamiltonian

In this subsection, we explain the details of the effective Hamiltonian in Eq. (1) in the present work. For the shell-model calculations within the  $fp$ -shell model space, the GXPF1A Hamiltonian [41] is often applied to reproduce and to predict the properties of nuclei in the region of  $Z$  or  $N$  from 20 to 40. Recently, the GXPF1A Hamiltonian has been improved to explain the observed energy levels in neutron-rich Ca isotopes: GXPF1B [42] with the modification of five  $T = 1$  two-body matrix elements and the bare single-particle energy which involve the  $1p_{1/2}$  orbit from GXPF1A, and GXPF1Br [7] with the modification of the monopole interaction for  $\langle 0f_{5/2}1p_{3/2} | V | 0f_{5/2}1p_{3/2} \rangle_{T=1}$  from GXPF1B. The GXPF1B Hamiltonian can reproduce the energy levels of  $^{51,52}\text{Ca}$ , and the GXPF1Br Hamiltonian can reproduce those of  $^{53,54}\text{Ca}$  besides  $^{51,52}\text{Ca}$ . Here, we adopt the newest effective Hamiltonian, GXPF1Br, for  $fp$ -shell orbits. For neutron  $1\hbar\omega$  excitation to the  $0g_{9/2}$  or  $1d_{5/2}$  orbits, we create the cross-shell two-body interaction between the  $fp$ -shell and  $gds$ -shell orbits from  $V_{\text{MU}}$  [43],

which has the central force of a simple Gaussian form and the tensor force of the  $\pi + \rho$  mesons exchange force to reproduce the monopole properties of the shell-model Hamiltonian in  $sd$  and  $fp$  shells. We utilize  $V_{\text{MU}}$  with the refinement [44] by adding the M3Y spin-orbit force [45] and the density dependence for the central force described in [46]. All two-body matrix elements are scaled by  $(A/42)^{-0.3}$  as the mass dependence.

In addition to the cross-shell two-body interaction, the bare single-particle energies with the  $^{40}\text{Ca}$  inert core for the  $0g_{9/2}$  and  $1d_{5/2}$  orbits need to be determined. The bare single-particle energy of  $0g_{9/2}$  is determined so as to reproduce the excitation energy of  $9/2_1^+$  states systematically. However, determining the bare single-particle energy of  $1d_{5/2}$  is more difficult than that of  $0g_{9/2}$ . The single-particle property of the  $1d_{5/2}$  orbit in this mass region is masked. In fact, the experimental spectroscopic factors of the  $5/2_1^+$  state in neutron-rich odd-mass Cr and Fe nuclei are rather small in comparison with those of the  $9/2_1^+$  state [47–49]. Here, we assume that the bare single-particle energy of  $1d_{5/2}$  is equal to that of  $0g_{9/2}$ . This assumption is considered to be reasonable because the splitting of the effective single-particle energies between  $0g_{9/2}$  and  $1d_{5/2}$  for nuclei taken in this study, around 2 MeV, is close to the phenomenological  $gds$ -shell orbits splitting in this mass region [50]. In the present work, the bare single-particle energy of  $0g_{9/2}$  (= that of  $1d_{5/2}$ ) is determined so as to be fitted to reproduce the excitation energies of  $9/2_1^+$  in  $^{55,57,59}\text{Cr}$ . The resulting value is 0.793 MeV.

Figure 1 shows the energy levels of  $^{57}\text{Cr}$  and the results of the shell-model calculations with the above mentioned Hamiltonian. As seen in Fig. 1, the  $fp$  shell-model calculation with GXPF1Br reproduces the negative(natural)-parity states quite well and GXPF1Br +  $V_{\text{MU}}$  without modification reproduces the positive(unnatural)-parity states reasonably well. For further improvement, we change the cross-shell two-body matrix elements by  $-1.0$  MeV for  $\langle 0g_{9/2}0f_{5/2} | V | 0g_{9/2}0f_{5/2} \rangle_{J=2,3,T=1}$  and by  $+1.0$  MeV for  $\langle 0g_{9/2}0f_{5/2} | V | 0g_{9/2}0f_{5/2} \rangle_{J=6,7,T=1}$ . This modification increases the energy intervals in the positive-parity band by about 15% as a whole. These results labeled GXPF1Br +  $V_{\text{MU}}(\text{modified})$  in Fig. 1 agree with the experimental data within  $\sim 500$  keV. In the following, we present the results for Cr and Fe isotopes with the new effective Hamiltonian, GXPF1Br +  $V_{\text{MU}}(\text{modified})$ .

### III. RESULTS AND DISCUSSION

#### A. Energy levels

The results of the present shell-model calculation with GXPF1Br +  $V_{\text{MU}}(\text{modified})$  are compared with the experimental data for Cr and Fe isotopes. We focus here on the lowest states for a given spin  $I$  and parity  $\pi = \pm$ . The results for odd-mass and even-mass nuclei are shown

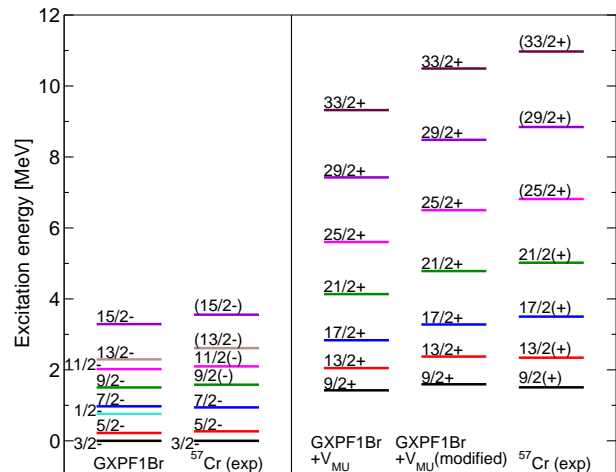


FIG. 1. (Color online) Shell-model results and experimental data of the energy levels of  $^{57}\text{Cr}$ . The experimental data labeled “ $^{57}\text{Cr}(\text{exp})$ ” are taken from [28].

in Figs. 2 and 3, respectively, where the unnatural-parity states are classified into two  $\Delta I = 2$  sequences.

For the odd-mass  $^{55-59}\text{Cr}$  and  $^{57-61}\text{Fe}$ , as seen in Fig. 2, the negative-parity states are described well by the shell-model calculation within the  $fp$ -shell model space. Furthermore, almost all of the observed positive-parity states are reproduced excellently by the present shell-model calculation. For the highest-spin  $37/2_1^+$  state in  $^{57}\text{Cr}$ , the backbending indicated by the small energy interval between the  $37/2_1^+$  and  $33/2_1^+$  [51] is not well reproduced in this calculation. This shows the limitation of description within the present model space and truncation. The theoretical results show that the  $1/2_1^+$  and  $5/2_1^+$  states lie at higher energy than the  $9/2_1^+$  state in each nucleus. This means that each  $9/2_1^+$  state is the lowest state in its band. Actually, the  $9/2_1^+$  and  $5/2_1^+$  states observed in  $^{55}\text{Cr}$  and  $^{57,59}\text{Fe}$  are almost degenerate. The present shell-model calculation predicts that the other positive-parity band including  $7/2_1^+$ ,  $11/2_1^+$ , ... is located higher than  $13/2_1^+$  in each nucleus.

For even-mass  $^{56,58}\text{Cr}$  and  $^{58,60}\text{Fe}$ , as seen in Fig. 3, the present calculation excellently describes the positive- and negative-parity states except for some of the high-spin states and the  $3_1^-$  states. The observed  $3_1^-$  states lie at slightly lower energies than the calculated ones, which may indicate that these  $3_1^-$  states are described not as a single particle-hole configuration but as collective states, for instance octupole vibrational states. The relative positions of the negative-parity odd- $I$  and even- $I$  bands are well reproduced with the present calculation. In  $^{58}\text{Fe}$ , for instance, the  $6_1^-$  and  $8_1^-$  levels are located higher than the  $7_1^-$  and  $9_1^-$  levels, respectively, whereas higher-spin states follow the regular ordering according to spin. In contrast, we predict that the  $\Delta I = 1$  partners such as  $6_1^-$  and  $7_1^-$  lie very close up to high-spin states for  $^{56}\text{Cr}$ .

One of the interesting features for these Cr and Fe nuclei is that the level spacing between  $\Delta I = 2$  of the band

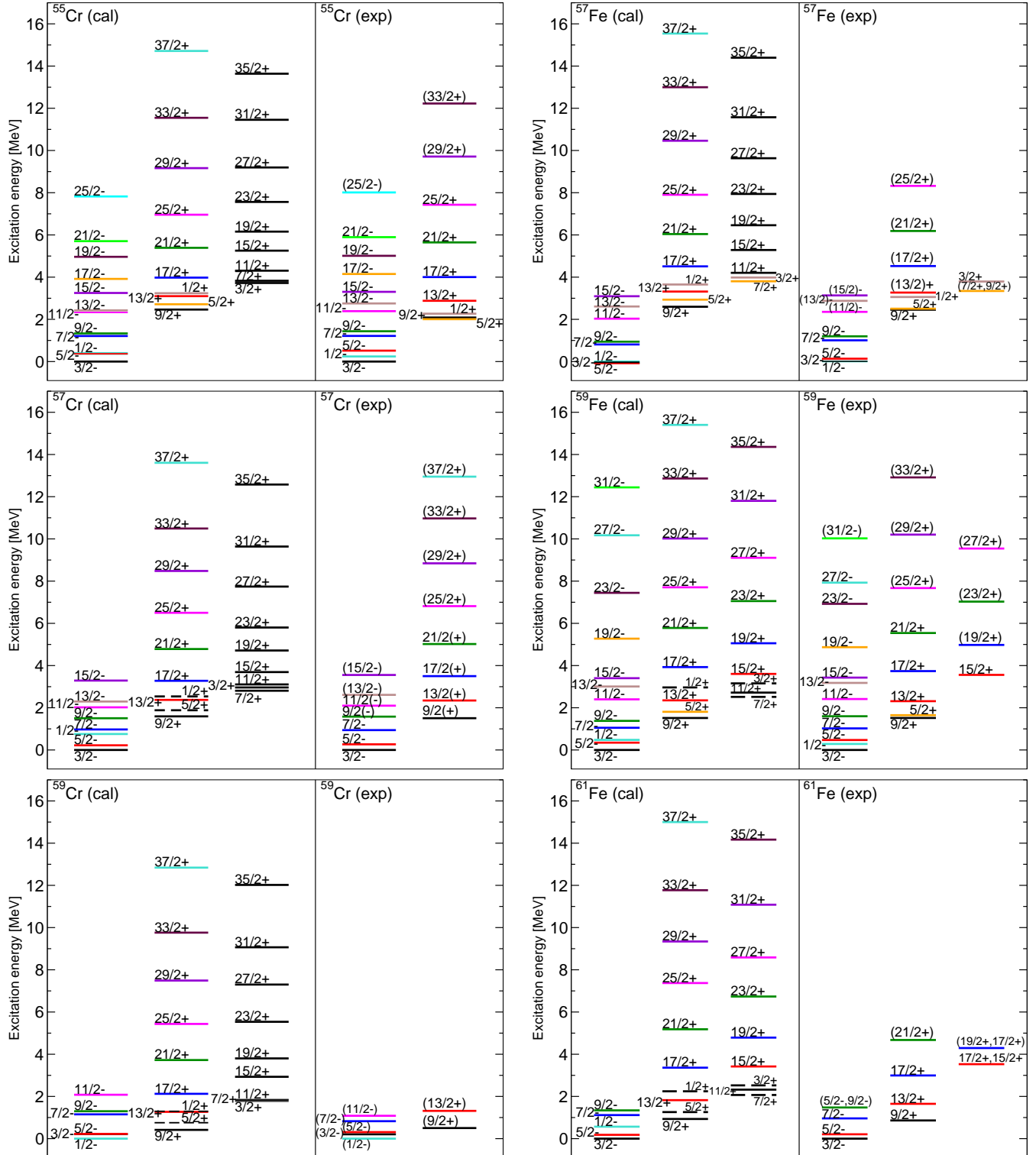


FIG. 2. (Color online) Calculated and experimental energy levels of the lowest states for each spin and parity in odd-mass Cr and Fe isotopes. In each panel, the left and right present the calculated and experimental energy levels, respectively. The experimental data are taken from [28–32, 47–49, 51].

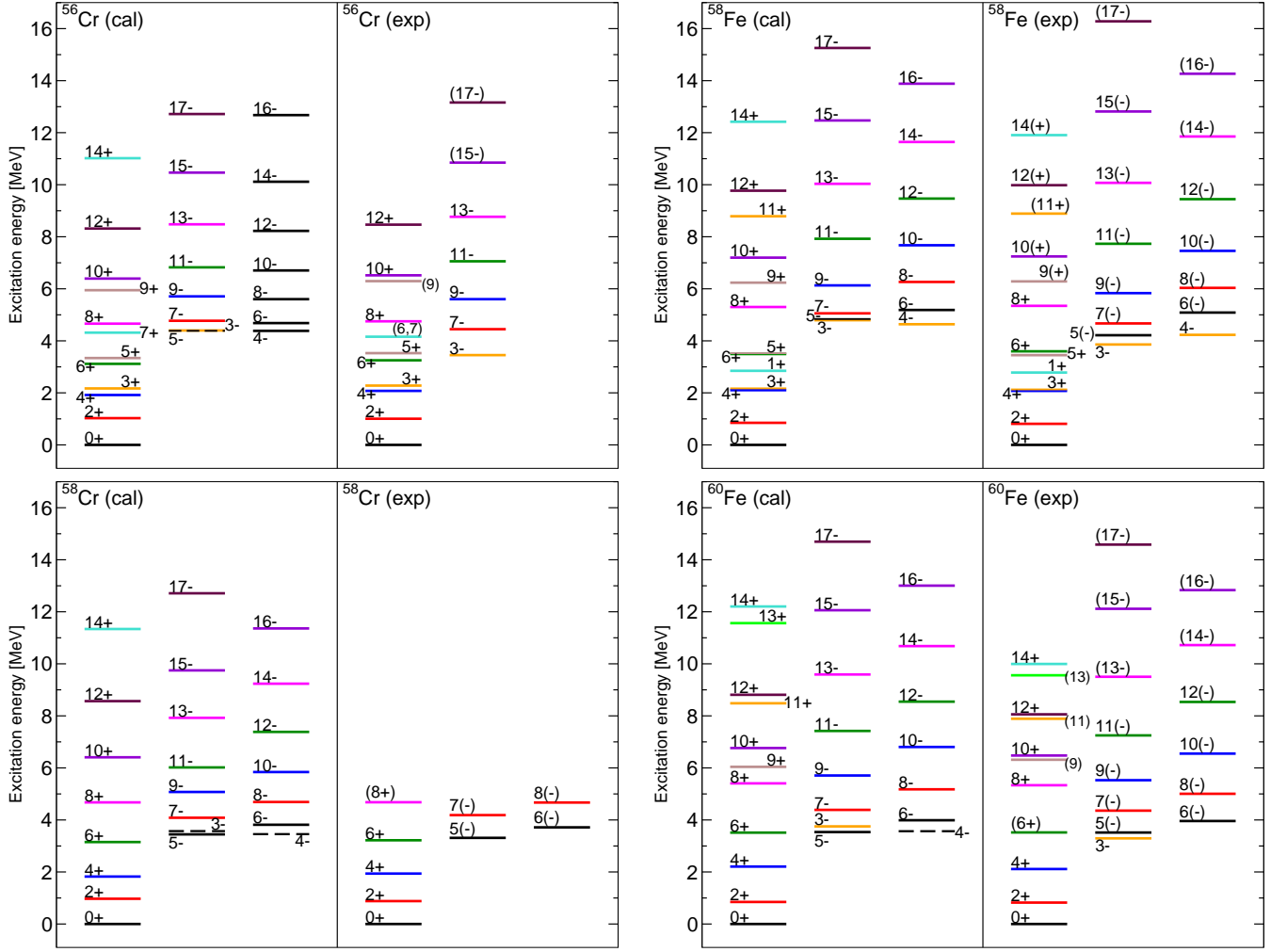


FIG. 3. (Color online) Calculated and experimental energy levels of the lowest states for each spin and parity in even-mass Cr and Fe isotopes. The notation is the same as in Fig. 2. The experimental data are taken from [30, 51–55]. In  $^{58}\text{Fe}$ , the experimental negative-parity states, except for the  $3_1^-$  and  $4_1^-$  states, are taken from Band 2 and 3 in [52], where these states are discussed based on the projected shell-model calculation [56] interpreting them as negative-parity states.

built on  $9/2_1^+$  in the odd-mass  $A$  nuclei is similar to that of the  $0_1^+$  band in the neighboring even-mass  $A - 1$  nuclei. For  $^{56-57,58-59}\text{Cr}$ , in Fig. 4, we compare the level spacing of the positive-parity yrast states between even- and odd-mass nuclei, which has already been discussed for  $^{54-55}\text{Cr}$  [27] and  $^{56-57,58-59,60-61}\text{Fe}$  [31]. One can see the similar level spacing between the yrast band in even-mass nuclei and the band of the  $9/2_1^+$  in odd-mass nuclei. Although the experimental information for the high-spin states in  $^{59}\text{Cr}$  is not enough, the present calculation predicts this similarity of the level spacing between  $^{58-59}\text{Cr}$ . This level structure indicates the decoupling limit of the particle-plus-rotor model [57, 58] as discussed in the next subsection.

## B. Deformations

In this subsection, we discuss the deformations for natural- and unnatural-parity states in neutron-rich Cr and Fe nuclei in terms of their intrinsic quadrupole moments. There is no straightforward way to determine the intrinsic quadrupole moments with the shell-model calculations because the shell-model wave functions are described in the laboratory frame. Here we probe deformations from two different approaches. One is approximating the wave function in the intrinsic frame. The other is extracting intrinsic deformations from shell-model wave functions using the geometric model.

The intrinsic-frame approximation in the shell model is often performed with the  $Q$ -constrained Hartree-Fock method [59, 60]. This method is, however, not suitable for deducing intrinsic wave functions for unnatural-parity states which are usually located higher than natural-

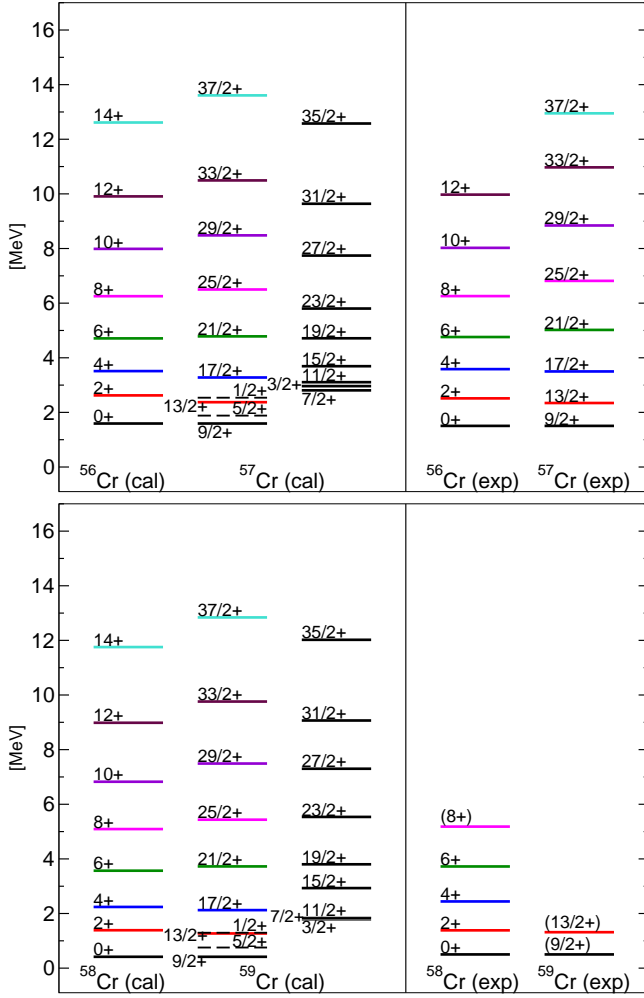


FIG. 4. (Color online) Comparison between the level spacing of the yrast bands in  $^{56,58}\text{Cr}$  and the bands built on  $9/2_1^+$  in  $^{57,59}\text{Cr}$ .

parity states. In the present study, we calculate the total energy surfaces separately for positive- and negative-parity states by performing the  $Q$ -constrained Hartree-Fock calculation with variation after parity projection. We utilize the parity-projected wave function  $|\Phi^\pi\rangle$  written as

$$|\Phi^\pi\rangle = \frac{1 + \pi\Pi}{2} |\Phi\rangle, \quad |\Phi\rangle = \prod_i \left( \sum_l^{N_s} D_{li} c_l^\dagger \right) |-\rangle, \quad (2)$$

where  $\Pi$  represents the space-reflection operator,  $\pi$  denotes the parity,  $\pi = \pm$ ,  $N_f$  and  $N_s$  represent the numbers of the valence particles and the single-particle orbits in the model space, respectively, and  $|-\rangle$  denotes an inert core. The coefficients  $D$  in  $|\Phi\rangle$  of Eq. (2) are determined to minimize the energy  $\langle \Phi^\pi | H | \Phi^\pi \rangle / \langle \Phi^\pi | \Phi^\pi \rangle$  with the constraints of quadrupole moments  $\langle Q_0 \rangle = \langle \Phi^\pi | Q_0 | \Phi^\pi \rangle / \langle \Phi^\pi | \Phi^\pi \rangle$  and  $\langle Q_2 \rangle = \langle \Phi^\pi | Q_2 | \Phi^\pi \rangle / \langle \Phi^\pi | \Phi^\pi \rangle$ , where the intrinsic axes are chosen to satisfy  $\langle \Phi^\pi | Q_{\pm 1} | \Phi^\pi \rangle = 0$ .  $Q_\mu$  is the  $\mu$  component of the mass quadrupole operator. Note that the wave

function of Eq. (2) is solved by using the shell-model Hamiltonian.

The total energy surfaces for the negative- and positive-parity states in odd-mass  $^{55-59}\text{Cr}$  and  $^{57-61}\text{Fe}$  are shown in Fig. 5. Those energy surfaces indicate the dominance of prolate deformation. For the negative-parity states, the quadrupole moments at the energy minima are around  $100 \text{ fm}^2$ . For the positive-parity states, those values are enlarged to be around  $120 \text{ fm}^2$ . The wave functions near the energy minima of the positive-parity energy surfaces are dominated by the excitation of one neutron into the  $0g_{9/2}$  orbit. This confirms the validity of the truncation of the model space introduced in this study. While the one-neutron excitation into the  $0g_{9/2}$  orbit induces larger deformation by  $\sim 20\%$ , the shape is not changed significantly. In  $^{59}\text{Cr}$ , the energy surfaces are  $\gamma$ -soft for both negative- and positive-parity states. In  $^{61}\text{Fe}$ ,  $\gamma$ -softness is seen for the positive-parity state. For the positive-parity state of  $^{59}\text{Fe}$ , triaxiality is well developed.

The situation of the even-mass Cr and Fe nuclei is very similar to that of the odd-mass nuclei as seen in Fig. 6. These energy surfaces indicate the dominance of prolate deformation. For the negative-parity states in even-mass nuclei, larger prolate deformations are induced by the excitation of one neutron into the  $\nu 0g_{9/2}$  orbit. In  $^{58}\text{Fe}$ , triaxiality is developed for both the positive- and negative-parity states as suggested by the  $\gamma$ -vibrational band [52, 61]. In  $^{60}\text{Fe}$ , triaxiality is developed for the negative-parity state.

The intrinsic quadrupole moment  $Q_0$  can also be deduced from the spectroscopic quadrupole moment  $Q_S$  by assuming the  $K$  quantum number [50] as

$$Q_S = \frac{3K^2 - I(I+1)}{(I+1)(2I+3)} Q_0, \quad (3)$$

where  $I$  denotes the spin of the state.  $Q_S$  is an observable and is also calculated directly by the shell model. We calculate  $Q_S$  with the effective charges  $e_\pi = 1.5e$  and  $e_\nu = 0.5e$ . The results for the band members starting from  $9/2_1^+$  are shown in Fig. 7, together with the experimental data for the  $9/2_1^+$  state in  $^{61}\text{Fe}$  [36]. The calculation reasonably reproduces the measured value. It should be noted that the magnetic moment of this state  $-1.031(9)\mu_N$  [35] is also close to the calculated value  $-0.934\mu_N$  using the free-nucleon  $g$  factors.

Since  $Q_0$  is identical among the members of an ideal rotor, the stability of  $Q_0$  within a band provides a key to determining the intrinsic state. Here, we take the two possibilities of  $K$  for the band members built on  $9/2_1^+$ :  $K = 1/2$  and  $9/2$  correspond to prolate and oblate shapes, respectively. Figure 7 shows the intrinsic quadrupole moment  $Q_0$  assuming  $K = 1/2$  for odd-mass nuclei  $^{55-59}\text{Cr}$  and  $^{57-61}\text{Fe}$ . As seen in Fig. 7, the  $Q_0$  value is nearly constant in Cr isotopes, whereas it decreases for high-spin states in Fe isotopes. This decrease might be due to change in shape or  $K$  number, as suggested by the predicted backbending in the  $29/2_1^+$  of



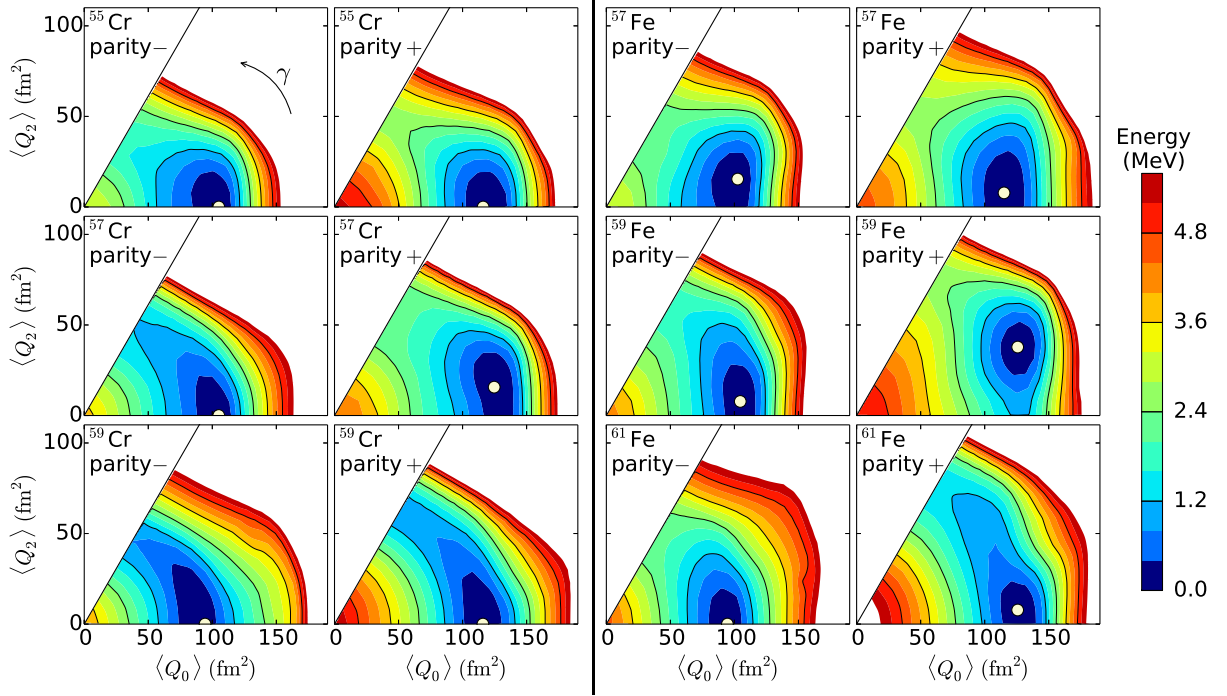


FIG. 5. (Color online) Total energy surfaces for the negative(natural)- and positive(unnatural)-parity states in odd-mass nuclei. The energy minima are represented by the points of open circles. The energy contours are based on the energy minima starting from 0 MeV.

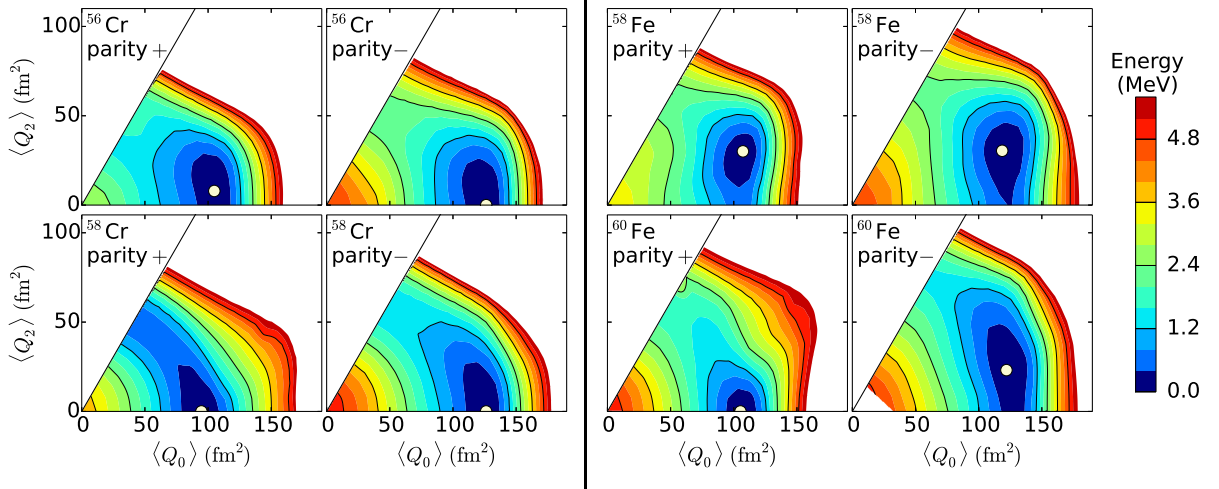


FIG. 6. (Color online) The total energy surfaces for the positive(natural)- and negative(unnatural)-parity states in even-mass nuclei. The notations are the same as in Fig. 5.

$^{61}\text{Fe}$  (see Fig. 2). If  $K = 9/2$  is assumed, on the other hand, we find a singular behavior of the  $Q_0$  value for each nucleus: the  $Q_0$  value is about  $-600 e \text{ fm}^2$  in the  $13/2_1^+$  state and it suddenly transits into the large positive value of about  $600 e \text{ fm}^2$  in the  $17/2_1^+$  state.

The intrinsic quadrupole moment  $Q_0$  is also connected to the  $B(E2, I \rightarrow I - 2)$  value [50]:

$$B(E2, I \rightarrow I - 2) = \frac{5}{16\pi} (\langle IK20 | I - 2 K \rangle)^2 Q_0^2, \quad (4)$$

where  $\langle IK20 | I - 2 K \rangle$  denotes the Clebsch-Gordan coefficient. Note that the sign of  $Q_0$  cannot be determined using Eq. (4). We calculate the  $B(E2)$  values with the same effective charges as the ones used for  $Q_S$ . The lowest panels of Fig. 7 show the absolute values of  $Q_0$  solved by Eq. (4) under the assumptions of  $K = 1/2$  and  $K = 9/2$ . The present calculation reproduces the experimental  $B(E2, 13/2_1^+ \rightarrow 9/2_1^+)$  in  $^{59}\text{Fe}$ . Similar to  $Q_S$ , the  $B(E2)$  values lead to much more stable intrinsic quadrupole moments with  $K = 1/2$  than with  $K = 9/2$ .

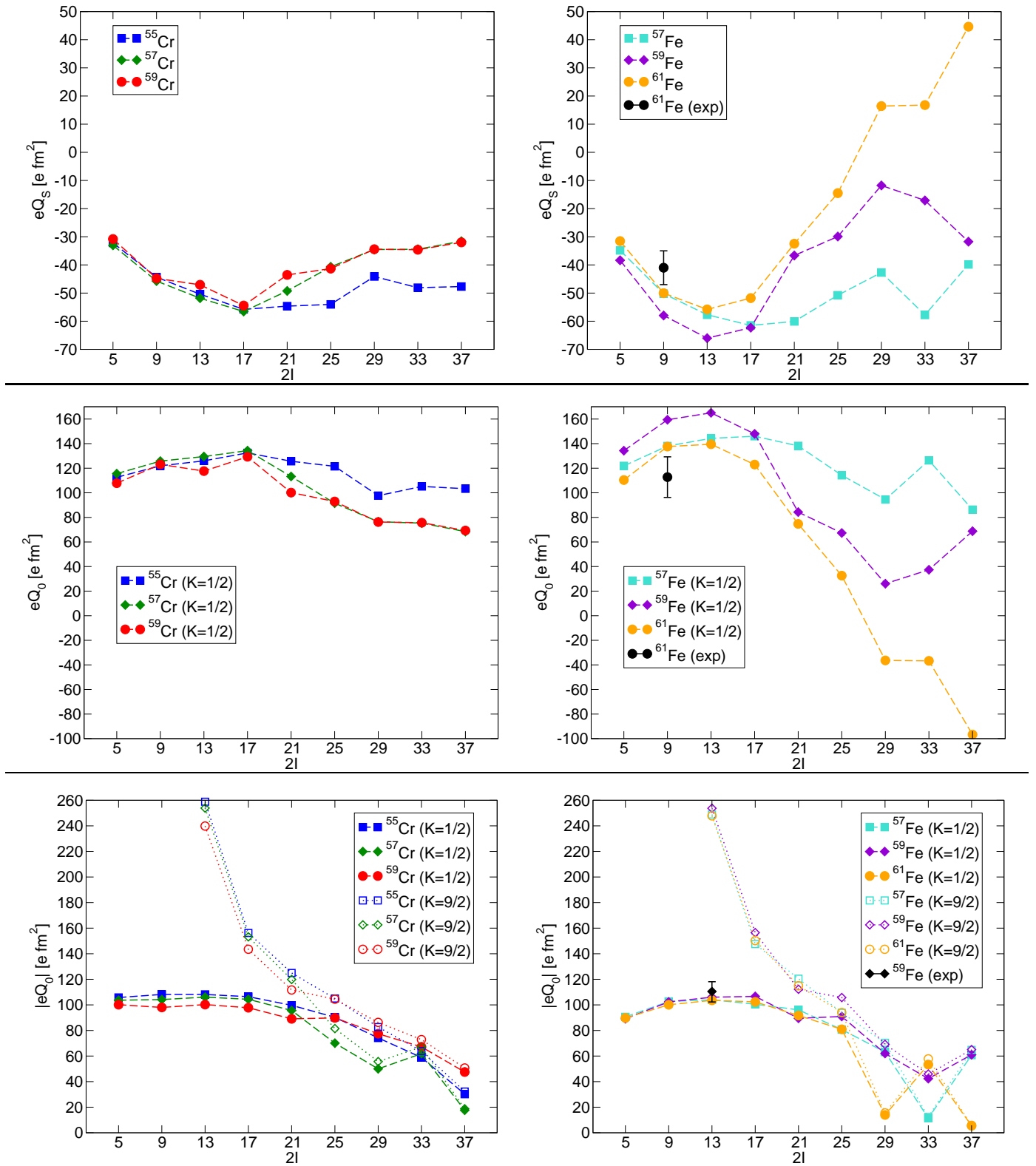


FIG. 7. (Color online) The electric spectroscopic and intrinsic quadrupole moments for the members of the band built on  $9/2_1^+$  in odd-mass Cr and Fe nuclei. The horizontal axes denote the spin  $I$  values of the states as  $2I$ . The upper panels show the electric spectroscopic quadrupole moments  $Q_S$ . The middle and lower panels show the intrinsic quadrupole moments  $Q_0$  solved by Eq. (3) assuming  $K = 1/2$  and the absolute values of  $Q_0$  solved by Eq. (4), respectively. The experimental spectroscopic quadrupole moment  $Q_S$  of  $^{61}\text{Fe}$  [36] labeled “ $^{61}\text{Fe}(\text{exp})$ ” is assumed to be negative. The absolute value of  $Q_0$  labeled “ $^{59}\text{Fe}(\text{exp})$ ” is evaluated with the experimental  $B(E2)$  values [49] assuming  $K = 1/2$ .



Although the mixing of the  $K$  quantum numbers occurs in reality due to the Coriolis effect, the present calculation supports the dominance of  $K = 1/2$  rather than  $K = 9/2$  and thus prolate deformation for the odd-mass Cr and Fe nuclei studied.

We point out here that the overall prolate deformation in the positive-parity states of  $^{55,57,59}\text{Cr}$  and  $^{57,59,61}\text{Fe}$  is indeed suggested by the measured energy levels, according to the analysis of the particle-plus-rotor model presented in [57, 58]. It is quite reasonable to apply the particle-plus-rotor model in which the last neutron occupies the  $j = 9/2$  orbit because the  $9/2_1^+$  states of those nuclei have rather large  $\nu 0g_{9/2}$  spectroscopic factors as presented in the next section. The level structure realized by the particle-plus-rotor model strongly depends on the strength of the Coriolis term relative to the  $\Omega^2$  term (originating from the Nilsson levels and recoil term), where  $\Omega$  is the projection of the angular momentum  $j$  of a orbit onto the symmetry axis. We here consider the case where the  $j$  orbit is occupied by the last nucleon alone. For oblate deformation having the maximum  $\Omega (= j)$ , the Coriolis term is less dominant because its matrix element is proportional to  $(j(j+1) - \Omega^2)^{1/2}$ . The energy levels then follow the strong-coupling limit of  $I(I+1)/2\mathcal{I}$  ( $I = \Omega, \Omega+1, \Omega+2, \dots$ ), where  $\mathcal{I}$  is the moment of inertia. For prolate deformation, on the other hand, the Coriolis term can dominate over the  $\Omega^2$  term especially when a high- $j$  orbit is involved. The energy levels in this case follow the decoupling limit of  $(I-\alpha)(I-\alpha+1)/2\mathcal{I}$ , where  $\alpha$  is the projection of  $j$  onto the rotation axis. The lowest-lying states take the largest possible  $\alpha$ . Since symmetry considerations require  $I - \alpha$  to be even, favored states with  $\alpha = j$  consist of  $I = j, j+2, j+4, \dots$  and unfavored states with  $\alpha = j-1$  consist of  $I = j+1, j+3, j+5, \dots$ . As a result, two major differences arise between prolate and oblate shapes. One is that the splitting of the favored and unfavored states is seen only for prolate deformation. The other is that energy spacings in the  $I = j, j+2, j+4, \dots$  levels are identical with those of even-even core,  $0^+, 2^+, 4^+, \dots$ , for prolate deformation but are much wider for oblate deformation. Those differences are also obtained from a microscopic calculation using the projected shell model [34]. The observed levels shown in Figs. 2 and 4 clearly support the decoupling limit which is realized for prolate deformation. Oblate deformation is quite unlikely but might not be completely excluded if deformation is small. Measuring unfavored states will provide additional information on shape.

#### IV. EVOLUTION OF THE $\nu 0g_{9/2}$ ORBIT

In this section, we examine what causes the sharp drop of the  $9/2_1^+$  level with increasing neutron number observed in Cr and Fe isotopes. A particular attention is paid to the relation to the evolution of the  $\nu 0g_{9/2}$  orbit.

We first confirm the descriptive power of our approach. Figure 8 shows the results of the excitation energy of

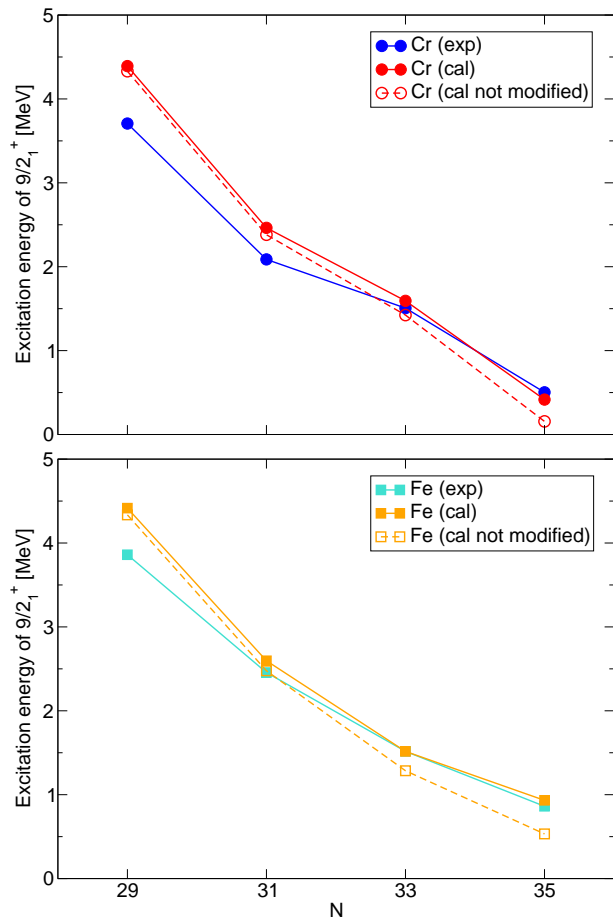


FIG. 8. (Color online) The excitation energy of  $9/2_1^+$  in odd-mass Cr and Fe isotopes from  $N = 29$  to  $N = 35$ . The plots labeled “(cal)” and “(exp)” represent the present results and the experimental data, respectively. The plots labeled “(cal not modified)” show the results without the modification of the two-body matrix elements described in Sec. II B. The experimental data are taken from [27–31, 47, 62]. In  $^{55}\text{Fe}$ , the state of 3.86 MeV excitation energy in [47] is adopted as the experimental  $9/2_1^+$  state because it has the largest spectroscopic factor of  $9/2_1^+$  in the  $(d, p)$  reaction.

$9/2_1^+$  from  $N = 29$  to  $N = 35$ . The sharp drop of  $9/2_1^+$  is reproduced quite well in the present calculations. Although the evolution of the  $9/2_1^+$  level is improved, as well as the high-spin levels, by the modification of the Hamiltonian introduced in Sec. II B, its basic trend is already seen without the modification. Thus, the  $V_{\text{MU}}$  interaction gives a reasonable evolution of the  $\nu 0g_{9/2}$  orbit, if the  $9/2_1^+$  levels are of single-particle origin.

The single-particle properties of the odd-mass Cr and Fe isotopes are probed from the spectroscopic factors for neutron transfer reactions. The measured spectroscopic factors are compared to the calculated values in Table I. While the experimental values scatter in some nuclei, the present calculation well reproduces their systematic behavior:  $\sim 0.5$  for the  $9/2_1^+$  states and  $0.1\text{--}0.2$  for the  $5/2_1^+$  states. This indicates that these  $9/2_1^+$  states are

TABLE I. Spectroscopic factors of  $\nu 0g_{9/2}$  and  $\nu 1d_{5/2}$  particle states for  $9/2_1^+$  and  $5/2_1^+$ , respectively. The experimental values labeled “exp” are taken from the data of the  $(d, p)$  reaction [63–71], the  $(\alpha, {}^3\text{He})$  reaction [72], and the  $({}^7\text{Li}, {}^6\text{Li})$  reaction [73]. Experimental excitation energies of  $5/2_1^+$  in  ${}^{53}\text{Cr}$  and  ${}^{55}\text{Fe}$  are 4.13 MeV and 4.46 MeV, respectively. Calculated excitation energies of  $5/2_1^+$  are 5.09 MeV and 5.19 MeV for  ${}^{53}\text{Cr}$  and  ${}^{55}\text{Fe}$ , respectively.

	cal		exp	
	$C^2S(9/2_1^+)$	$C^2S(5/2_1^+)$	$C^2S(9/2_1^+)$	$C^2S(5/2_1^+)$
${}^{53}\text{Cr}$	0.564	0.161	0.520 [63]	0.090 [63]
${}^{55}\text{Cr}$	0.458	0.142	0.67 [64]	0.225 [64]
			0.582 [65]	0.145 [65]
			-	0.17 [66]
${}^{57}\text{Cr}$	0.479	0.148	-	-
${}^{59}\text{Cr}$	0.498	0.152	-	-
${}^{55}\text{Fe}$	0.568	0.117	0.74 [67]	0.172 [67]
			-	0.13 [68]
${}^{57}\text{Fe}$	0.494	0.120	0.375 [72]	-
			0.67 [73]	0.25 [73]
			0.270 [69]	0.110 [69]
${}^{59}\text{Fe}$	0.442	0.113	0.447 [70]	0.114 [70]
			0.510 [71]	0.128 [71]
${}^{61}\text{Fe}$	0.527	0.133	-	-

the single-particle-like states but that the  $5/2_1^+$  states are not. Hence, the excitation energy of  $9/2_1^+$  in these nuclei is influenced directly by the location of the  $\nu 0g_{9/2}$  orbit.

Neutron effective single-particle energies (ESPEs) [74] in Cr and Fe isotopes are displayed in Fig. 9 using the present Hamiltonian. The ESPEs of  $\nu 0g_{9/2}$  are rather constant with increasing neutron number, and so are the shell gaps between the  $fp$  shell and  $\nu 0g_{9/2}$ . This indicates that the evolution of the  $9/2_1^+$  level is explained by the Fermi surface approaching the  $\nu 0g_{9/2}$  orbit with increasing neutron number. This is in contrast to the result of a previous shell-model study [20] in which this evolution occurs due to the lowering of the  $0g_{9/2}$  orbit. This lowering was realized in [20] by shifting the  $T = 1$  monopole interaction between  $0p_{3/2}$  and  $0g_{9/2}$  by  $-1.0$  MeV. It should be noted that the  $T = 1$   $j \neq j'$  monopole matrix elements in realistic interactions are in general rather small [43].

The evolution of the  $\nu 0g_{9/2}$  orbit can be probed from experimental energies. Namely, in the independent-particle limit, the  $\nu 0g_{9/2}$  single-particle energy is identical with the energy of the  $9/2_1^+$  state measured from the adjacent even-even core nucleus,  $-S_n + E_x(9/2_1^+)$ . This idea can be extended to deformed single-particle energies. In Fig. 10, the  $-S_n + E_x(9/2_1^+)$  values are compared between the experimental data and the present calculation. The observed stabilities in  $-S_n + E_x(9/2_1^+)$  along the Cr and Fe isotopic chains suggest that the  $\nu 0g_{9/2}$  single-particle energies are kept nearly constant as shown in Fig. 9.

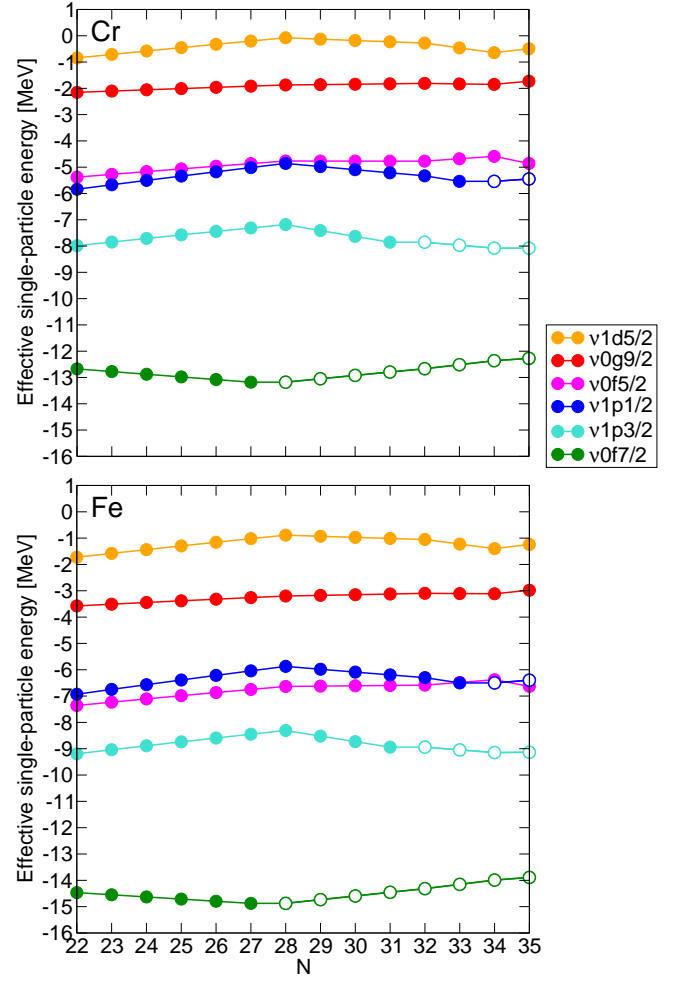


FIG. 9. (Color online) The effective single-particle energies (ESPEs) of a neutron for Cr and Fe isotopes. The open circles represent the ESPEs calculated as the hole states to specify the occupied states.

## V. CONCLUSIONS

We have investigated unnatural-parity high-spin states in neutron-rich Cr and Fe isotopes by large-scale shell-model calculations for the model space of  $fp$ -shell +  $0g_{9/2}$  +  $1d_{5/2}$  orbits with the truncation allowing  $1\hbar\omega$  excitation of a neutron. The effective Hamiltonian is composed of GXPF1Br for  $fp$ -shell orbits and a modified  $V_{\text{MU}}$  for the other parts. The shell-model calculations with the present Hamiltonian can describe and predict the energy levels of both natural- and unnatural-parity states up to the high-spin states in Cr and Fe isotopes with  $N \leq 35$ . This shell-model calculation has shown that the  $9/2_1^+$  states are the lowest positive-parity states in the odd-mass nuclei and the level spacings of the bands built on  $9/2_1^+$  in the odd-mass  $A$  nuclei are similar to those of the  $0_1^+$  bands in the neighboring even-mass  $A - 1$  nuclei.

We have also discussed the deformations of Cr and Fe isotopes by utilizing the  $Q$ -constrained Hartree-Fock

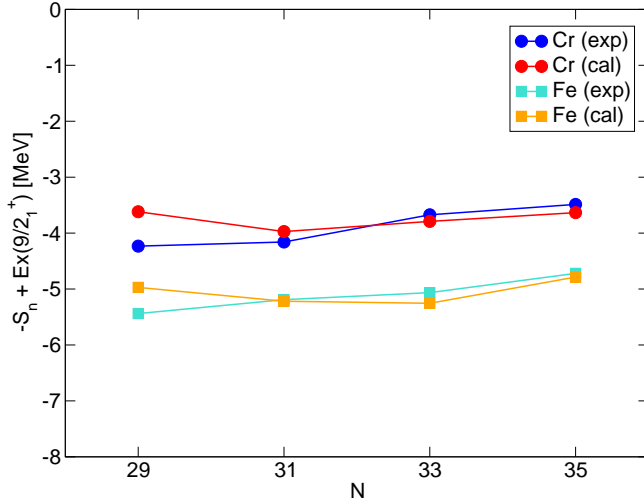


FIG. 10. (Color online) Plots of  $-S_n + E_x(9/2_1^+)$ . Experimental one-neutron separation energies  $S_n$  are taken from [47–49, 62, 75]. Coulomb energy is corrected in the calculated  $S_n$  according to [9].

calculation with variation after parity projection. This study has indicated that the present Cr and Fe nuclei have the prolate deformations on the whole. In these energy surfaces, the excitation of one neutron into the  $\nu 0g_{9/2}$  orbit plays the role of enhancing the prolate deformation. The electric intrinsic quadrupole moments  $Q_0$ , which are calculated by using the electric spectroscopic quadrupole moments  $Q_S$  and the  $B(E2)$  values obtained in the shell-model calculation, have supported the prolate deformations of the states in the band built

on  $9/2_1^+$  in odd-mass Cr and Fe nuclei and have indicated that their dominant  $K$  quantum number is  $1/2$ . This situation corresponds to the decoupling limit of the particle-plus-rotor model, which can explain the systematics of the positive-parity level schemes in these Cr and Fe nuclei.

In the present calculation, the effective single-particle energies of  $\nu 0g_{9/2}$  in Cr and Fe isotopes are rather constant in the region with  $N \leq 35$ , which means very weak attraction between the  $fp$ -shell orbits and  $0g_{9/2}$  orbit as given by  $V_{\text{MU}}$ . We have shown that this can be confirmed from the one-neutron separation energy ( $S_n$ ) and the excitation energy of  $9/2_1^+$  ( $E_x(9/2_1^+)$ ). This result indicates that the sharp drop of the  $9/2_1^+$  levels in the Cr and Fe nuclei in this mass region is explained by the Fermi surface approaching the  $\nu 0g_{9/2}$  orbit with the increase of neutron number.

## ACKNOWLEDGMENTS

This work was supported in part by MEXT SPIRE Field 5 “The origin of matter and the universe” and JICFuS. This research partly used the computational resources of the K computer provided by the RIKEN Advanced Institute for Computational Science through the HPCI System Research Project (Project ID:hp130024, hp140210), the FX10 supercomputer at the Information Technology Center at the University of Tokyo, and the computational resources of the RIKEN-CNS joint research project on large-scale nuclear-structure calculations.

- 
- [1] A. Huck *et al.*, Phys. Rev. C **31**, 2226 (1985).
  - [2] A. Gade *et al.*, Phys. Rev. C **74**, 021302(R) (2006).
  - [3] R. V. F. Janssens *et al.*, Phys. Lett. B **546**, 55 (2002).
  - [4] D.-C. Dinca *et al.*, Phys. Rev. C **71**, 041302(R) (2005).
  - [5] R. Chapman *et al.*, Nucl. Phys. A **119**, 305 (1968).
  - [6] A. Bürger *et al.*, Phys. Lett. B **622**, 29 (2005).
  - [7] D. Steppenbeck *et al.*, Nature **502**, 207 (2013).
  - [8] T. Otsuka *et al.*, Phys. Rev. Lett. **87**, 082502 (2001).
  - [9] M. Honma *et al.*, Phys. Rev. C **69**, 034335 (2004).
  - [10] E. Caurier *et al.*, Rev. Mod. Phys. **77**, 427 (2005).
  - [11] T. Otsuka *et al.*, Phys. Rev. Lett. **95**, 232502 (2005).
  - [12] R. Broda *et al.*, Phys. Rev. Lett. **74**, 868 (1995).
  - [13] T. Ishii *et al.*, Phys. Rev. Lett. **84**, 39 (2000).
  - [14] O. Sorlin *et al.*, Phys. Rev. Lett. **88**, 092501 (2002).
  - [15] B. Pritychenko *et al.*, At. Data Nucl. Data Tables **98**, 798 (2012).
  - [16] N. Aoi *et al.*, Phys. Rev. Lett. **102**, 012502 (2009).
  - [17] T. Baugher *et al.*, Phys. Rev. C **86**, 011305(R) (2012).
  - [18] H. L. Crawford *et al.*, Phys. Rev. Lett. **110**, 242701 (2013).
  - [19] W. Rother *et al.*, Phys. Rev. Lett. **106**, 022502 (2011).
  - [20] K. Kaneko *et al.*, Phys. Rev. C **78**, 064312 (2008).
  - [21] H. Oba and M. Matsuo, Prog. Theor. Phys. **120**, 143 (2008).
  - [22] S. M. Lenzi *et al.*, Phys. Rev. C **82**, 054301 (2010).
  - [23] A. Gade *et al.*, Phys. Rev. Lett. **112**, 112503 (2014).
  - [24] E. K. Warburton *et al.*, Phys. Rev. C **41**, 1147 (1990).
  - [25] Y. Utsuno *et al.*, Phys. Rev. C **60**, 054315 (1999).
  - [26] Y. Tsunoda *et al.*, Phys. Rev. C **89**, 031301(R) (2014).
  - [27] D. E. Appelbe *et al.*, Phys. Rev. C **67**, 034309 (2003).
  - [28] A. N. Deacon *et al.*, Phys. Lett. B **622**, 151 (2005).
  - [29] S. J. Freeman *et al.*, Phys. Rev. C **69**, 064301 (2004).
  - [30] A. N. Deacon *et al.*, Phys. Rev. C **76**, 054303 (2007).
  - [31] N. Hoteling *et al.*, Phys. Rev. C **77**, 044314 (2008).
  - [32] A. N. Deacon *et al.*, Phys. Rev. C **83**, 064305 (2011).
  - [33] G. A. Lalazissis *et al.*, Nucl. Phys. A **628**, 221 (1998).
  - [34] Y.-C. Yang *et al.*, Phys. Lett. B **700**, 44 (2011).
  - [35] I. Matea *et al.*, Phys. Rev. Lett. **93**, 142503 (2004).
  - [36] N. Vermeulen *et al.*, Phys. Rev. C **75**, 051302(R) (2007).
  - [37] A. P. Zuker *et al.*, Phys. Rev. C **52**, R1741 (1995).
  - [38] D. H. Gloeckner and R. D. Lawson, Phys. Lett. **53B**, 313 (1974).
  - [39] T. Mizusaki, N. Shimizu, Y. Utsuno, and M. Honma, private communications.
  - [40] N. Shimizu, arXiv:1310.5431.
  - [41] M. Honma *et al.*, Eur. Phys. J. A **25**, s01, 499 (2005).

- [42] M. Honma *et al.*, RIKEN Accelerator Progress Report **41**, 32 (2008).
- [43] T. Otsuka *et al.*, Phys. Rev. Lett. **104**, 012501 (2010).
- [44] Y. Utsuno *et al.*, Phys. Rev. C **86**, 051301(R) (2012).
- [45] G. Bertsch *et al.*, Nucl. Phys. A **284**, 399 (1977).
- [46] B. A. Brown *et al.*, Ann. Phys. **182**, 191 (1988).
- [47] H. Junde, Nucl. Data Sheets **109**, 787 (2008), and references therein.
- [48] M. R. Bhat, Nucl. Data Sheets **85**, 415 (1998), and references therein.
- [49] C. M. Baglin, Nucl. Data Sheets **95**, 215 (2002), and references therein.
- [50] A. Bohr and B. R. Mottelson, *Nuclear Structure vol. 2* (1975).
- [51] S. Zhu *et al.*, Phys. Rev. C **74**, 064315 (2006).
- [52] D. Steppenbeck *et al.*, Phys. Rev. C **85**, 044316 (2012).
- [53] H. Junde *et al.*, Nucl. Data Sheets **112**, 1513 (2011), and references therein.
- [54] C. D. Nesaraja *et al.*, Nucl. Data Sheets **111**, 897 (2010), and references therein.
- [55] E. Browne *et al.*, Nucl. Data Sheets **114**, 1849 (2013), and references therein.
- [56] Y. Sun *et al.*, Phys. Rev. C **80**, 054306 (2009).
- [57] P. Ring and P. Schuck, *The Nuclear Many-Body Problem* (1980).
- [58] F. S. Stephens, Rev. Mod. Phys. **47**, 43 (1975).
- [59] T. Mizusaki *et al.*, Phys. Rev. C **59**, R1846 (1999).
- [60] N. Shimizu *et al.*, Phys. Rev. C **85**, 054301 (2012).
- [61] S. Cavallaro *et al.*, Nucl. Phys. A **293**, 125 (1977).
- [62] H. Junde, Nucl. Data Sheets **110**, 2689 (2009), and references therein.
- [63] M. N. Rao *et al.*, Nucl. Phys. A **121**, 1 (1968).
- [64] R. Bock *et al.*, Nucl. Phys. **72**, 273 (1965).
- [65] A. E. Macgregor and G. Brown, Nucl. Phys. A **198**, 237 (1972).
- [66] T. Taylor and J. A. Cameron, Nucl. Phys. A **337**, 389 (1980).
- [67] R. H. Fulmer and A. L. McCarthy, Phys. Rev. **131**, 2133 (1963).
- [68] D. C. Kocher and W. Haeberli, Nucl. Phys. A **196**, 225 (1972).
- [69] H. M. S. Gupta *et al.*, Nucl. Phys. A **160**, 529 (1971).
- [70] J. A. Thomson, Nucl. Phys. A **227**, 485 (1974).
- [71] K. C. McLean *et al.*, Nucl. Phys. A **191**, 417 (1972).
- [72] P. Roussel *et al.*, Nucl. Phys. A **155**, 306 (1970).
- [73] O. Karban *et al.*, Nucl. Phys. A **535**, 377 (1991).
- [74] M. H. Storm *et al.*, J. Phys. G: Nucl. Phys. **9**, L165 (1983).
- [75] M. R. Bhat, Nucl. Data Sheets **88**, 417 (1999), and references therein.